PHYSICAL REVIEW X **10,** 041002 (2020)

Multiorbital Processes Rule the $Nd_{1-x}Sr_xNiO_2$ Normal State

Frank Lechermann

I. Institut für Theoretische Physik, Universität Hamburg, Jungiusstrasse 9, 20355 Hamburg, Germany

(Received 11 May 2020; revised 15 July 2020; accepted 19 August 2020; published 2 October 2020)

The predominant Ni-multiorbital nature of infinite-layer neodymium nickelate at stoichiometry and with doping is revealed. We investigate the correlated electronic structure of $NdNiO_2$ at lower temperatures and show that first-principles many-body theory may account for Kondo(-lattice) features. Yet, those features are not only based on localized Ni-$d_{x^2-y^2}$ and a Nd-dominated self-doping band, but they heavily build on the participation of Ni-d_{z^2} in a Hund-assisted manner. In a tailored three-orbital study, the half-filled regime of the former in-plane Ni orbital remains surprisingly robust even for substantial hole doping δ. Reconstructions of the interacting Fermi surface designate the superconducting region within the experimental phase diagram. Furthermore, they provide clues to recent Hall measurements, as well as to the astounding weakly insulating behavior at larger experimental δ. Finally, a strong asymmetry between electron and hole doping, with a revival of Ni single-orbital features in the former case, is predicted. Unlike cuprates, superconductivity in $Nd_{1-x}Sr_xNiO_2$ is of distinct multiorbital kind, building up on nearly localized Ni-$d_{x^2-y^2}$ and itinerant Ni-d_{z^2}.

DOI: 10.1103/PhysRevX.10.041002

Subject Areas: Condensed Matter Physics,
Strongly Correlated Materials,
Superconductivity

I. INTRODUCTION

The discovery of superconductivity in Sr-doped thin films of infinite-layer (IL) $NdNiO_2$ with a T_c in the 10-K range marks a further milestone in the investigation of transition-metal oxides [1]. Recent experimental works provide details on the thin-film growth on a $SrTiO_3$ substrate and, moreover, yield a phase diagram with doping [2–4]. There, the superconducting region is placed in the range $0.125 \lesssim x \lesssim 0.25$ within the $Nd_{1-x}Sr_xNiO_2$ system. Notably, that area is neighbored by weakly insulating regions on either side of the doping range. Not surprisingly, the original findings [1] were already covered by many theoretical works [5–29], with important earlier studies [30–33] on similar nickelate systems as well.

Up to now, three (interlinked) key questions are associated with the challenging physics of superconducting nickelates. The first one deals with the basic comparison to high-T_c layered cuprates. Though seemingly akin, IL nickelate [see Fig. 1(a)] with the unusual Ni^+ formal oxidation state shows prominent differences at stoichiometry: $NdNiO_2$ is weakly metallic and does not exhibit magnetic ordering down to the lowest measured temperatures [1]. Theoretical calculations furthermore show that it has an additional self-doping (SD) band crossing the Fermi level and that the charge-transfer character is weaker than in cuprates [11,15]. Second, strong correlations within the Ni-$d_{x^2-y^2}$ state, together with an existing SD band, raise the question about Kondo (-lattice) physics at low temperatures. An experimentally found [1] resistivity upturn below about $T \sim 70$ K might indeed be indicative of related processes. The third, highly debated question is most relevant for the superconducting mechanism, and it deals with the issue of deciding low-energy physics based on single-Ni-orbital processes of the Ni-$d_{x^2-y^2}$ kind [18–23] versus processes of the multi-Ni-orbital kind [7,9–11,31] at stoichiometry and with finite hole doping from replacing Nd by Sr.

In a previous work [11], we focused on the one-to-one comparison of IL nickelates with structurally akin cuprates. The present study uncovers crucial Ni-multiorbital mechanisms for Kondo physics at stoichiometry and for the accentuation of the superconducting region with hole doping.

First-principles many-body theory and a realistic three-band Hamiltonian investigation are utilized to establish our current understanding of IL nickelates. Besides the significance of Ni-$d_{x^2-y^2}$ and the Nd-dominated SD band, we unveil the decisive role of Ni-d_{z^2}, both for Kondo(-lattice) behavior at stoichiometry and for the characterization of the normal-state correlated electronic structure with hole doping δ. While the Ni-$d_{x^2-y^2}$ Fermi-surface sheet in the $k_z = 0$

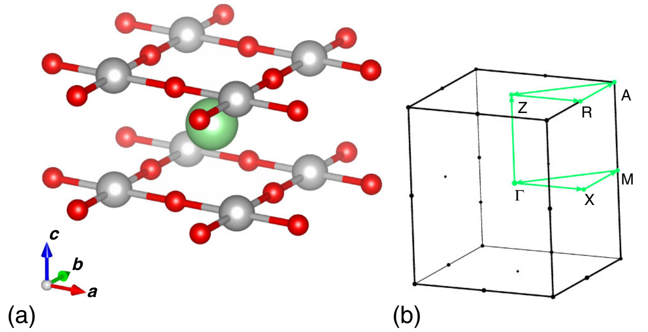

FIG. 1. Infinite-layer $NdNiO_2$. (a) Crystal structure with Nd (green), Ni (blue), and O (red) sites. (b) Brillouin zone with high-symmetry points in the $k_z = 0$ and $k_z = 1/2$ plane. Green lines depict the path for plots of the spectral function $A(\mathbf{k}, \omega)$.

plane hardly evolves with increasing δ, an additional Ni-d_{z^2} sheet becomes available in the $k_z = 1/2$ plane for dopings in the region of the onset of superconductivity. On the other hand, further changes of the Fermi surface at larger hole doping may be connected to the experimentally found, weakly insulating behavior. Furthermore, the given Fermi-surface reconstructions with doping are in line with the experimentally established Hall-data-based multiband picture of an evolution from electronlike to holelike transport. In a final step, we compare hole doping with theoretical electron doping and detect a stronger single-orbital character of Ni-$d_{x^2-y^2}$ flavor on the electron-doped side.

II. METHODS

In essence, three methodologies are put into practice in this work. First, the charge self-consistent combination [34] of density functional theory (DFT), self-interaction correction (SIC), and dynamical mean-field theory (DMFT), i.e., the so-called DFT + sicDMFT framework [35], is used to provide a realistic approach to the temperature-dependent correlated electronic structure of $NdNiO_2$. The complete Ni($3d$) shell enters the correlated subspace of the DMFT impurity problem. Coulomb interactions on oxygen are described within SIC and are incorporated in the O pseudopotential [36]. A mixed-basis pseudopotential code [37–39] takes care of the DFT part in the local density approximation (LDA). The SIC is applied to the O($2s$) and the O($2p$) orbitals via weight factors w_p (see Ref. [36] for more details). While the O($2s$) orbital is, by default, fully corrected with $w_p = 1.0$, the common choice [35,36] $w_p = 0.8$ is used for O($2p$) orbitals. Hence, the oxygen states are treated beyond conventional DFT + DMFT but still not on eye level with Ni($3d$). Cluster calculations for transition-metal oxides (e.g., Refs. [40–42]) have been put forward in this direction, but those schemes often suffer from other problems, such as, e.g., parametrization issues and breaking of translational invariance.

The Nd($4f$) states are placed in the pseudopotential frozen core since they appear irrelevant for the key physics of superconducting IL nickelates [21]. A continuous-time quantum Monte Carlo method in hybridzation expansion [43] as implemented in the TRIQS code [44,45] is utilized to address the DMFT problem. The DMFT correlated subspace is governed by a five-orbital full Slater Hamiltonian applied to the Ni projected-local orbitals [46]. The projection is performed on the $6 + 5 + 1 = 12$ Kohn-Sham states above the dominant O($2s$) bands, associated with O($2p$), Ni($3d$), and the self-doping band. A Hubbard $U = 10$ eV and a Hund's exchange $J_{\mathrm{H}} = 1$ eV prove reasonable for this large-energy window treatment of the given late transition-metal oxide [11]. The fully localized-limit double-counting (DC) scheme [47] is applied. The DFT + sicDMFT calculations are performed in the paramagnetic regime. Maximum-entropy and Padé methods are employed for the analytical continuation from Matsubara space to the real-frequency axis. Stoichiometric lattice parameters are taken from experiment [1].

Second, we employ the maximally localized Wannier-function (MLWF) formalism [48,49] to construct an effective three-orbital low-energy Hamiltonian for $NdNiO_2$, which will be utilized at stoichiometry and with finite doping. Details of the construction are provided in Sec. IV A.

Third, the derived Hamiltonian is solved by the rotationally invariant slave-boson (RISB) scheme [50–55] on the mean-field level. The RISB electronic self-energy is local (or extendable via cluster techniques) and consists of a term that is linear in frequency as well as a static part. Thus, it lacks the full frequency dependence of the DMFT self-energy, but it is still well suited (here, at formal $T = 0$) for a large class of correlated materials problems. For details on the computation of quantities such as the quasiparticle (QP) weight Z or local spin correlations, see, e.g., Refs. [51,54].

III. KONDO SIGNATURE IN $NdNiO_2$ FROM COMPREHENSIVE REALISTIC DMFT

In Ref. [11], we studied the interacting electronic structure of $NdNiO_2$ using the DFT + sicDMFT method at the system temperature $T = 193$ K. At the reasonable large interaction strength $U = 10$ eV, the half-filled Ni-$d_{x^2-y^2}$ band is Mott insulating and does not participate in the Fermi surface. This case is shown in Fig. 2(a), where only the electron pockets of the self-doping band cross the Fermi level ε_F in the $k_z = 0$ plane around Γ and in the $k_z = 1/2$ plane around A. The SD band is of mixed Ni-Nd character, namely, Nd-$d_{z^2,xy}$ and an especially relevant Ni-d_{z^2} contribution to the Γ pocket [11,19]. A more detailed discussion of the orbital hybridizations can be found in Ref. [11].

At lower temperatures, a coupling of the localized Ni-$d_{x^2-y^2}$-based spin-1/2 and the remaining itinerant degrees of freedom is suggested from the strong-coupling

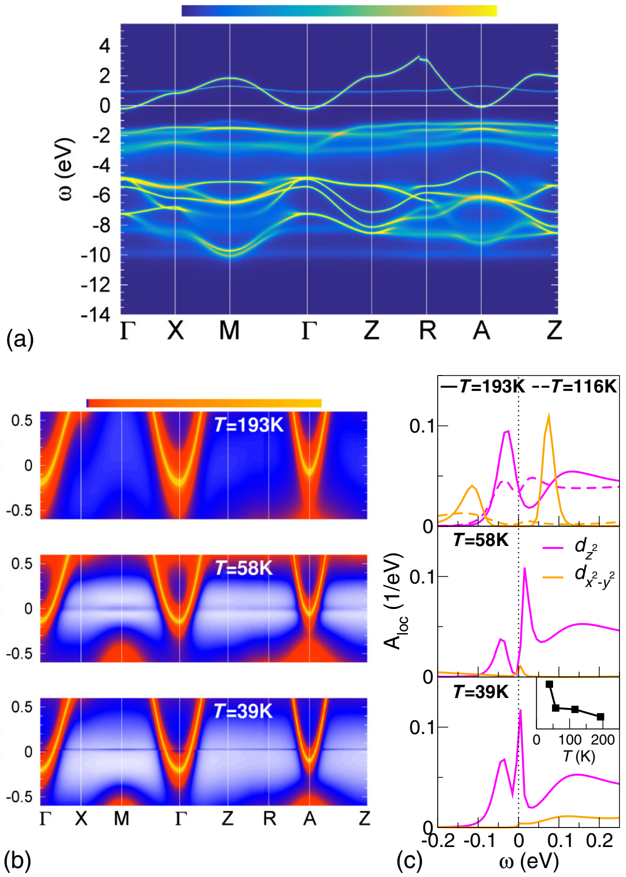

FIG. 2. Evolution of the DFT + sicDMFT spectral data for $\mathrm{NdNiO_2}$ with decreasing temperature. (a) **k**-resolved spectrum $A(\mathbf{k},\omega)$ along high-symmetry lines in the Brillouin zone over a wide energy range at $T = 193$ K (from Ref. [11]). (b) Low-energy $A(\mathbf{k},\omega)$ for three different temperatures. (c) T-dependent Ni-d_{z^2} and Ni-$d_{x^2-y^2}$ local spectral function A_{loc} close to the Fermi level. The small inset in the bottom part shows the two-orbital integrated spectral weight in the energy window $[-0.05, 0.05]$ eV.

situation. An underscreening scenario is then expected because of the low filling of the electron pockets. But importantly, there is zero nearest-neighbor hopping between Ni-$d_{x^2-y^2}$ and Nd-$d_{z^2,xy}$ (e.g., Ref. [11]). Thus, an intriguing Kondo(-lattice) picture is expected. Note, however, that it is computationally challenging to reach very low temperatures within our five-Ni-orbital realistic DMFT framework.

Still, Fig. 2(b) displays the evolution of the **k**-resolved correlated electronic structure at low energy with decreasing T. At $T = 58$ K, a flat-dispersion feature appears in the spectral function $A(\mathbf{k},\omega)$ close to ε_F, which further settles below 40 K. The location of the electron pockets of the SD band remains rather T independent. It is very tempting to link this lowest-energy crossing of a flat-band feature and itinerant, seemingly weakly correlated dispersions, to a Kondo scenario. Yet, the spectral intensity of the flat feature remains very weak at these reachable temperatures. The orbital-resolved local spectrum depicted in Fig. 2(c) renders it obvious that the main Ni-derived spectral weight in this region is of Ni-d_{z^2} character. At $T = 193$ K, a single Ni-d_{z^2} quasiparticle peak is located just below ε_F at about -30 meV. Lowering the temperature first leads to a second peak above the Fermi level that gradually becomes sharper and shifts towards ε_F. Hence, the "Kondo resonance" property, at least in that T range, is carried by the Ni-d_{z^2} character, which points to a relevant participation of Ni-d_{z^2} in the given low-energy physics. The local spectral weight of the Ni-e_g kind near ε_F strongly grows below $T = 58$ K [see inset at bottom in Fig. 2(c)], in good agreement with the experimental temperature scale for the onset of the resistivity increase. The orbital-resolved electron count is hardly dependent on T, and it reads $\{n_{z^2}, n_{x^2-y^2}\} = \{1.845, 1.065\}$ for Ni.

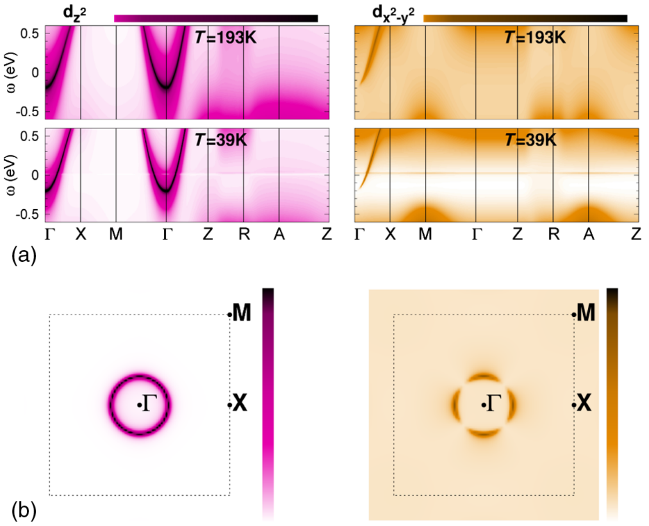

FIG. 3. Orbitals weights (i.e., "fat-band" picture) for Ni-d_{z^2} (left) and Ni-$d_{x^2-y^2}$ (right) character in the **k**-resolved DFT + sicDMFT spectrum of $\mathrm{NdNiO_2}$. (a) Along high-symmetry lines in the Brillouin zone at $T = 193$ K and $T = 39$ K. (b) On the Fermi surface in the $k_z = 0$ plane at $T = 193$ K. Note that the Ni-d_{z^2} color-scale maximum is 30 times larger than the Ni-$d_{x^2-y^2}$ one.

To investigate the roles of the two Ni-e_g orbitals further, we also extracted their **k**-resolved orbital characters (i.e., fat bands) in the interacting regime, as shown in Fig. 3(a). First, it is once more confirmed that there is no Ni-e_g contribution to the electron pocket around A. Second, the Ni-$d_{x^2-y^2}$ orbital weight at low energy is much smaller than the Ni-d_{z^2} one. The Ni-$d_{x^2-y^2}$ origin of the flat feature at low T is still obvious. Third, the Ni-$d_{x^2-y^2}$ orbital displays a low-energy hybridization with Ni-d_{z^2} within the Γ pocket; however, interestingly, it is only along $\Gamma - X$ in the chosen Brillouin-zone path. This specific direction-dependent hybridization is clearly visible already at $T = 193$ K, and by close inspection, it is even observable on the

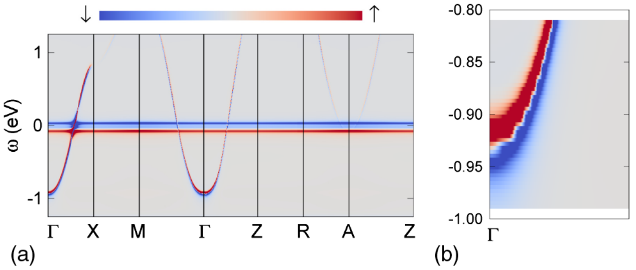

FIG. 4. Spin contrast $A_{\uparrow}(\mathbf{k},\omega) - A_{\downarrow}(\mathbf{k},\omega)$ from a one-step DFT + sicDMFT calculation with spin-polarized Ni self-energies (see text). (a) Energy window around the Fermi level. (b) Blow-up close to Γ, to extract the spin splitting of the electron pocket.

LDA level. Its structure is yet better revealed when plotting the Ni-$d_{x^2-y^2}$ orbital weight along the $k_z = 0$ Fermi surface [see Fig. 3(b)]. The corresponding weight is strictly zero along $\Gamma - X$, and along $\Gamma - Z$ from Fig. 3(a). Since the oxygen positions in real space correspond to the $\Gamma - X$ direction, we attribute this Ni-Ni hybridization to explicit hopping via oxygen. It appears relevant for the present Kondo scenario since it provides the sole, explicit Ni-d_{z^2} connection between the single level and the Γ pocket at lower temperatures [cf. Fig. 3(a)]. As an inspection below $T = 58$ K, a Fermi-surface maximum on the circular sheet appears along $\Gamma - X$ and splits perpendicular to the $\Gamma - X$ direction, respectively (not shown).

In order to eventually also connect to the spin degree of freedom in the simplest manner, we choose a linear-response(-kind) calculation. For $T = 39$ K, we strongly spin split the paramagnetic Ni-$d_{x^2-y^2}$ occupation by hand and perform a single DFT + sicDMFT step allowing for spin-polarized Ni self-energies. This one-step "magnetic-order" calculation leads to a spin contrast in the low-energy spectral function as shown in Fig. 4(a). As expected, the single level, mirroring the localized-spin behavior, is split into a larger-occupied spin-up branch and a smaller-occupied spin-down part (due to the spin splitting performed by hand). However, the effect of this splitting on the itinerant pockets is important since it may deliver information about the Kondo(-like) exchange coupling. First, the A pocket shows only a weak spin signature. Yet, the Γ pocket displays sizable spin splitting and hence is Kondo affected by the localized Ni-$d_{x^2-y^2}$ spin. As one can easily see, the pocket's spin splitting is the other way around; i.e., the spin-up band is shifted to somewhat higher energies, which indeed points to an antiferromagnetic (AFM) exchange coupling between Ni-$d_{x^2-y^2}$ and the SD band.

The size of the SD spin splitting at Γ amounts to 40 meV [see Fig. 4(b)], which translates into a Kondo coupling as $J_{\mathrm{K}} \sim 120$ meV. This value is quite large for J_{K} but indeed in agreement with recent estimates [21,56]. Notably, a Ni-d_{z^2} supported AFM exchange is not in contradiction with Hund's first rule. In fact, in the regime of highly occupied Ni-d_{z^2}, a *local* $S = 1$ triplet from d_{z^2} and $d_{x^2-y^2}$ favors an additional *itinerant* d_{z^2}, which is AFM aligned to $d_{x^2-y^2}$. As a final observation, the spin-contrast signal is highlighted at the $\Gamma - X$ crossing of the single level and the Γ pocket, underlining, once more, the relevant Ni-d_{z^2} role.

IV. LOW-ENERGY STUDY OF THE CORRELATED ELECTRONIC STRUCTURE

To proceed on the electronic states in IL nickelates in a more general and flexible way, let us turn to an explicit low-energy description, where we focus on a minimal set of degrees of freedom that are essential for the key electronic processes at lower temperatures. For instance, the nearly completely filled Ni-t_{2g} states are fully included in the DFT + sicDMFT study, yet in a first step, their effect on the essential physics at low energy may be cast into a formulation based on integrating out those orbital degrees of freedom.

A. Minimal Hamiltonian

For the selection of the truly relevant degrees of freedom in an unbiased manner, it makes sense to be guided by the previous, more comprehensive DFT + sicDMFT picture. From the results of Ref. [11] and those of Sec. III, the natural conclusion has to be that we definitely need Ni-d_{z^2}, Ni-$d_{x^2-y^2}$, and the SD band. The SD band carries important weight from Nd-$d_{z^2,xy}$, which amounts to a four-orbital Hamiltonian. This result is not unfeasible, but one wonders if it is truly "minimal" also in a model sense for general IL nickelates. For instance, we learned that the A pocket, where the Nd-orbital contribution is most substantial [11], is apparently not as important as the Γ pocket in the low-temperature interacting regime. Therefore, it may be sufficient for a truly minimal setting to merge the Nd($5d$) part at low energy with the remaining Ni-t_{2g}, Ni($4s$), and O($2p$) contributions and ally them altogether in a "stand-alone bath" degree of freedom coupled to the Ni-e_g orbitals.

We thus arrive at a three-orbital Hamiltonian, based on Ni-d_{z^2}, Ni-$d_{x^2-y^2}$, and a third orbital, which we still call SD, but it understandably now carries all the non-Ni-e_g contributions at low energy. Concretely, the complete Hamiltonian reads

$$H_{\mathrm{min}} = H_{\mathrm{kin}} + \sum_i (H_{\mathrm{int}}^{(i)} + H_{\mathrm{orb}}^{(i)}), \qquad (1)$$

using the label i for the unit cell. It incorporates the kinetic part H_{kin}, the local-interacting part H_{int}, and a further local, orbital contribution H_{orb}. The kinetic Hamiltonian, here liberated from all local terms, may be written with hoppings t as

$$H_{\mathrm{kin}} = \sum_{i\neq j,mm',\sigma} t_{ij,mm'} c^{\dagger}_{im\sigma} c_{jm'\sigma}, \tag{2}$$

where $m, m' = \text{Ni-}d_{z^2}, \text{Ni-}d_{x^2-y^2}, \text{SD}$, and $\sigma = \uparrow, \downarrow$. For H_{int}, we choose a canonical Slater-Kanamori form to describe local interactions among the Ni-e_g orbitals, i.e.,

$$\begin{aligned} H^{(i)}_{\mathrm{int}} = U &\sum_{m=z^2,x^2-y^2} n_{m\uparrow} n_{m\downarrow} + \sum_{\sigma} \{ U' n_{z^2\sigma} n_{x^2-y^2\bar{\sigma}} \\ &+ U'' n_{z^2\sigma} n_{x^2-y^2\sigma} + J_{\mathrm{H}} c^{\dagger}_{z^2\sigma} c^{\dagger}_{x^2-y^2\bar{\sigma}} c_{z^2\bar{\sigma}} c_{x^2-y^2\sigma} \\ &+ J_{\mathrm{H}} c^{\dagger}_{z^2\sigma} c^{\dagger}_{z^2\bar{\sigma}} c_{x^2-y^2\bar{\sigma}} c_{x^2-y^2\sigma} \}, \end{aligned} \tag{3}$$

and $U' = U - 2J_{\mathrm{H}}$, $U'' = U - 3J_{\mathrm{H}}$. Thus, notably within the present choice, explicit interactions within the SD orbital, or between Ni-e_g and SD, are set to zero in our minimal realistic modeling. The final H_{orb} not only deals with the local sum $\varepsilon^{\mathrm{loc}}$ of kinetic energies but, importantly, also has to take care of double counting due to a depiction of strongly interacting Ni-e_g coupled to a weakly interacting SD state. Furthermore, the SIC description in the DFT + sicDMFT calculations addresses relevant interactions on O($2p$) in this late transition-metal oxide, which now also enters the double-counting term. Therefore, it proves favorable in this minimal context to split the DC correction into two parts: a negative shift of the SD state through a potential μ_{SD} in the interacting case, and a standard DC correction for explicitly interacting Ni-e_g. For the latter, we again choose the fully localized-limit form [47]. The last term in Eq. (1) is hence given by

$$\begin{aligned} H^{(i)}_{\mathrm{orb}} = &\sum_{mm',\sigma} \varepsilon^{\mathrm{loc}}_{mm'} c^{\dagger}_{m\sigma} c_{m'\sigma} - \mu_{\mathrm{SD}} \sum_{\sigma} n_{\mathrm{SD}\sigma} \\ &- \sum_{m=z^2,x^2-y^2} \left[U\left(\tilde{n}_{e_g} - \frac{1}{2}\right) - J_{\mathrm{H}}\left(\tilde{n}_{e_g\sigma} - \frac{1}{2}\right) \right] n_{m\sigma}. \end{aligned} \tag{4}$$

As we will utilize the minimal Hamiltonian without charge self-consistency, the $\tilde{n}$ occupations in Eq. (4) refer to e_g fillings at $U = 0$ (in the following, "$U = 0$" is understood as $U = J_{\mathrm{H}} = 0$). The potential μ_{SD} for the SD state is not perfectly straightforward since therein we accumulate various effects, such as electrostatics, interaction with O($2p$), etc. Since NdNiO$_2$ for the present minimal three-orbital Hamiltonian is located at total half-filling $n = 3$, the most canonical choice is provided by $\mu_{\mathrm{SD}} = U/2$ (e.g., Ref. [57]).

For a concrete representation of the Hamiltonian form described, maximally localized Wannier functions are derived from the LDA electronic structure. For instruction, Fig. 5 shows the LDA Fermi surface of NdNiO$_2$ with its three distinct sheets, namely, the larger Ni-$d_{x^2-y^2}$-dominated sheet as well as the pocket sheets around Γ and around A. Because of the strong downfolding to three orbitals, the disentangling procedure [49] is employed, and the twofold dispersion closest to the Fermi surface is fixed in an inner energy window. The result of this Wannier construction is displayed in Fig. 6. The overall Wannier dispersion agrees well with the LDA one, and the fat-band analysis clearly identifies the Ni-d_{z^2}, Ni-$d_{x^2-y^2}$, and SD bands. The dispersions and fat bands around point A are hard to align exactly within the present orbital setting, which can be easily understood from the fact that the occupied part of this very region has a sizable contribution from Ni-t_{2g}. However, again, from our more general DFT + sicDMFT description, the very details around the A point

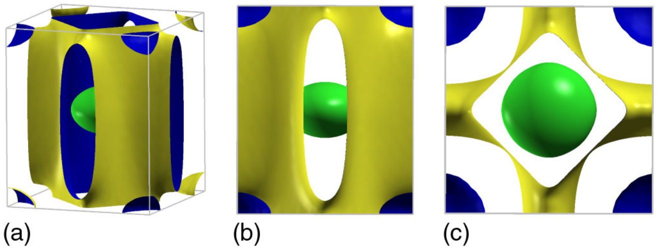

FIG. 5. LDA Fermi surface of pristine NdNiO$_2$. (a) 3D view, (b) view along k_x, and (c) view along k_z.

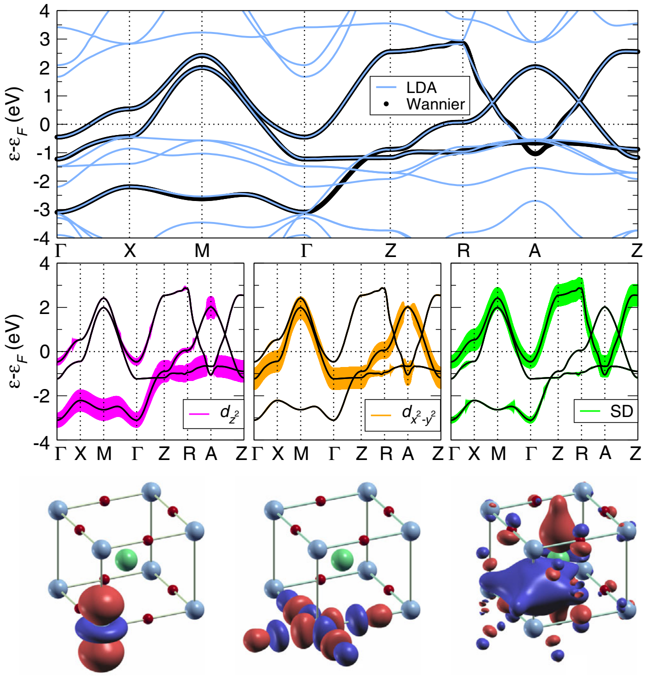

FIG. 6. Wannier properties of the three-band model for IL nickelate. Top panel: Low-energy LDA bands of NdNiO$_2$ (light blue) and Wannier dispersion (black) along high-symmetry lines in the Brillouin zone. Middle panels: Orbital weights on the Wannier dispersion (i.e., fat-band picture); from left to right: Ni-d_{z^2}, Ni-$d_{x^2-y^2}$, and SD orbital. Bottom panels: Constant-value surfaces of the three Wannier orbitals (aligned as in the middle row).

are not crucial for the IL nickelate physics. It also becomes clear from Fig. 6 that other DFT bands in the energy window around $[-2,-1]$ eV are not included in the minimal description, and therefore, it does not resemble a true "monotonic" low-energy Hamiltonian. However, this case is tailored to the present problem and "backed up" by the full-fledged DFT + sicDMFT study: The DFT bands left out are of dominant Ni-t_{2g} character and remain, to a good approximation, filled spectators throughout the phase diagram (see also the comment in Sec. V).

But, importantly, note that the present SD orbital not only describes the electron pockets at Γ and A but also has nonzero orbital weight on the Ni-e_g-dominated dispersions, mostly on the Ni-d_{z^2} band. This fact is generally very relevant to appreciate the role of Ni-d_{z^2} and to understand the following results with doping.

The real-space Wannier orbitals are shown in the bottom part of Fig. 6. For Ni-e_g, they resemble the expected appearance. Substantial leaking of Ni-$d_{x^2-y^2}$ onto in-plane oxygen sites is a natural outcome of the strong downfolding. Of course, by construction, here the SD orbital cannot resemble an atomiclike orbital; since it is not based on a highly localized viewpoint, its spread is comparatively large and the Wannier center is in between Ni and Nd. It has contributions from Nd, Ni, and O and furthermore breaks the full-cubic symmetry. This orbital is important for its "stand-alone" features coupled to Ni-e_g.

Let us conclude this subsection by providing the Wannier values for the local single-particle terms $\varepsilon^{\mathrm{loc}}$ and for near hoppings t in Table I. The nearest-neighbor hopping between Ni-$d_{x^2-y^2}$ and SD, here notably included in $\varepsilon^{\mathrm{loc}}$, is indeed zero, but there is a sizable one between Ni-d_{z^2} and SD.

B. RISB solution

The paramagnetic RISB solution of the minimal Hamiltonian H_{min} in the stoichiometric half-filled case and with finite doping is discussed. Technically speaking, the present multiorbital Hamiltonian is solved in a "cluster-RISB" fashion since the on-site Ni-e_g effects and the intersite effects between Ni-e_g and the SD orbital are treated on equal footing.

TABLE I. Local single-particle terms and selected hoppings of the derived Wannier Hamiltonian. All energies are in meV.

Orbitals	$\varepsilon^{\mathrm{loc}}$	$t_{12}^{(x)}$	$t_{12}^{(z)}$	$t_{13}^{(x)}$
Ni-d_{z^2}, Ni-d_{z^2}	−1479	−1	−398	0
Ni-$d_{x^2-y^2}$, Ni-$d_{x^2-y^2}$	232	−387	−30	−50
SD, SD	1191	−13	−229	12
Ni-d_{z^2}, SD	92	125	77	−8
Ni-d_{z^2}, Ni-$d_{x^2-y^2}$	0	41	0	9
Ni-$d_{x^2-y^2}$, SD	0	17	0	13

1. Stoichiometry

Pristine NdNiO$_2$ resembles the half-filled $n=3$ case of the three-orbital description. At $U=0$, the orbital fillings read $\{n_{z^2}, n_{x^2-y^2}, n_{\mathrm{SD}}\} = \{1.84, 0.93, 0.23\}$; i.e., the Ni-$d_{x^2-y^2}$ orbital lies somewhat below true half-filling. Figure 7(a) shows the evolution of key quantities of the low-energy electronic structure with increasing Hubbard U. Be aware that due to the strong downfolding, the lack of charge self-consistency, as well as the RISB treatment, the tailored U value surely differs from $U=10$ eV of the DFT + sicDMFT study.

As U grows from zero, charge transfers occur such as to establish a truly half-filled Ni-$d_{x^2-y^2}$ orbital in an orbital-selective Mott transition scenario. For $U=7$ eV, the fillings read $\{n_{z^2}, n_{x^2-y^2}, n_{\mathrm{SD}}\} = \{1.83, 1.0, 0.17\}$, and

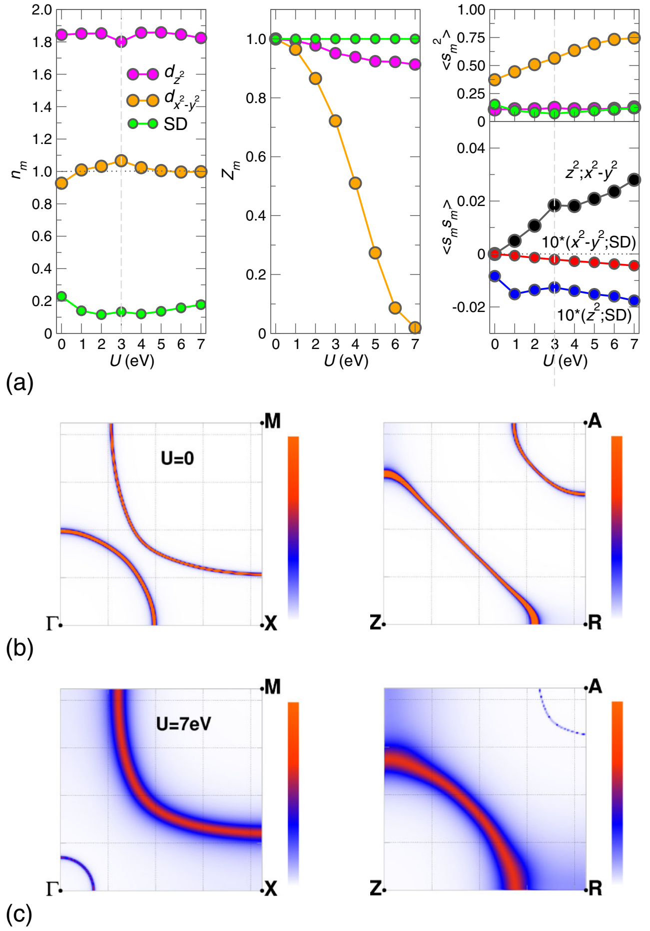

FIG. 7. Minimal-Hamiltonian properties at half-filling for $\mu_{\mathrm{SD}} = U/2$. (a) Selected quantities for increasing U. The Hund's exchange is chosen as $J_{\mathrm{H}} = U/3$ for $U < 3$ and fixed to $J_{\mathrm{H}} = 1$ eV for $U \geq 3$ eV (the dashed gray line separates the regimes). From left to right: Orbital occupation n_m, orbital-resolved QP weight, and local squared-spin moment (top), as well as local spin-spin correlation (bottom). (b) Noninteracting Fermi surface for $k_z = 0$ (left) and $k_z = 1/2$ (right). (c) Interacting Fermi surface for $U = 7$ eV.

the QP weight Z (i.e., the inverse effective mass) of the in-plane orbital reads $Z_{x^2-y^2} = 0.02$, i.e., is close to zero. In the following, we will understand the electronic states at $U = 7$ eV as the low-energy equivalent to the more comprehensive DFT + sicDMFT picture at $U = 10$ eV. The QP weight Z_{z^2} remains close to unity due to the rather large filling. The localization of the Ni-$d_{x^2-y^2}$ electron is accompanied by the buildup of a corresponding local squared spin moment $\langle s^2 \rangle$, which saturates at the limiting value $s(s+1/2) = 3/4$. The Ni-e_g spin-spin correlations are surely positive because of Hund's first rule, and they increase with a localization degree of Ni-$d_{x^2-y^2}$. On the other hand, the intersite spin-spin correlations of the $\{\text{Ni-}e_g, \text{SD}\}$ kind are negative and much smaller in magnitude. The $\{\text{Ni-}d_{z^2}, \text{SD}\}$ spin correlations are still larger than the $\{\text{Ni-}d_{x^2-y^2}, \text{SD}\}$ ones, which again proves that a *direct* spin-spin coupling between the latter orbitals is weak.

In view of the dichotomy between itinerant and localized behavior in strongly correlated materials, let us further focus on Fermi surfaces and local states. The noninteracting Fermi surface in Fig. 7(b) shows the electron pockets around Γ and A, as well as the Ni-$d_{x^2-y^2}$-dominated sheet in the $k_z = 0, 1/2$ planes. Note the closing of the latter sheet along Z-R as a difference from conventional cuprate fermiology (see Ref. [25] for a direct comparison). In the strongly interacting case, the Γ pocket shrinks, and since the QP at $U = 7$ eV is not yet exactly zero, the strongly renormalized Ni-$d_{x^2-y^2}$ sheet still contributes to the Fermi surface (yet it is now slightly enlarged due to the exact half-filling). But in the $k_z = 1/2$ plane, the near-Mott-insulating sheet apparently bends electronlike. The warping close to $k_z = 1/2$ is therefore further strengthened with strong correlations. We will not comment further on the small-A-pocket features because of possible Wannier-construction artifacts in that region for $U \neq 0$.

The slave-boson amplitudes $\phi_{qq'}$ connecting states q, q' in the RISB formalism provide useful insight in the local-state behavior for different degrees of electronic correlation. Let us first note the corresponding Hilbert space. There are a total of $2^6 = 64$ (Fock) states available for our three-orbital system, with each particle sector $N = 0, \ldots, 6$ contributing $N_q = 6!/(N!(6-N)!)$ states. Thus, if coupling between *all* states is allowed, the total number of $\phi_{qq'}$ amounts to $64 \times 64 = 4096$ for a three-orbital problem. However, here, we only study normal-state properties and therefore exclude couplings between different particle sectors. A RISB implementation for pairing problems also permitting such couplings has been put forward by Isidori and Capone [52]. Without pairing, one ends up with $\sum_N N_q^2 = 924$ slave-boson amplitudes (without using symmetries) in the RISB calculation. The squared amplitudes of the relevant part of those are depicted in Fig. 8 for the noninteracting case and for $U = 7$ eV. The values $|\phi_{qq'}|^2$ may be interpreted as the weight for finding the system in a quantum state characterized by q, q' to occur since $\sum_{qq'} |\phi_{qq'}|^2 = 1$ holds. There is, of course, the option to transfer from a Fock basis to a multiplet basis [54], but because of the specific itinerant intersite structure of our Hamiltonian, we remain in the Fock basis for a straightforward analysis.

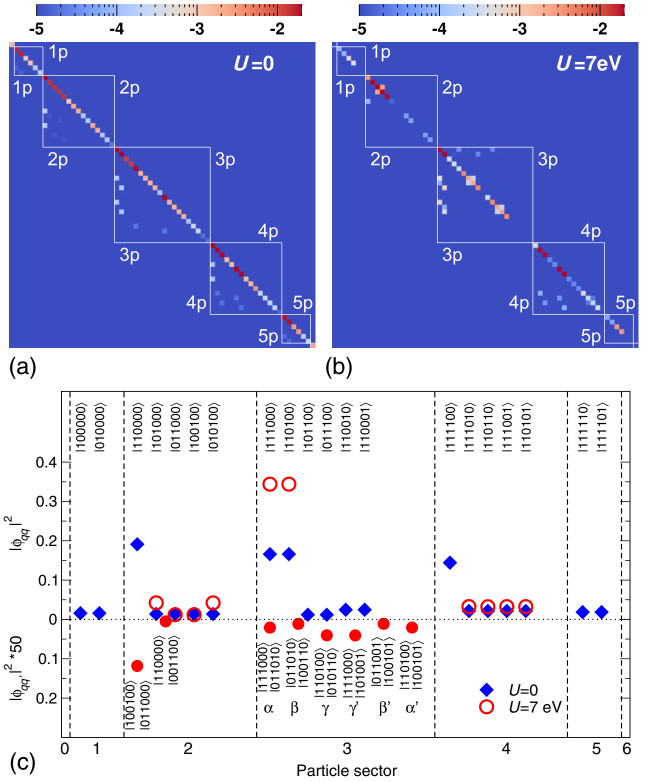

FIG. 8. Local-state behavior of the minimal Hamiltonian via the slave-boson weights $|\phi_{qq'}|^2$ connecting Fock states q, q'. (a,b) Weight matrix in q, q'-space covering the $N = 0, \ldots, 6$ particle sectors Np for weights greater than 10^{-5}: (a) $U = 0$ and (b) $U = 7$ eV. (c) Dominant diagonal weights (along the positive axis) for $U = 0$ and for $U = 7$ eV, and dominant off-diagonal weights (along the negative axis) within each particle sector for $U = 7$ eV (filled circles).

Figures 8(a) and 8(b) first show that for sizable magnitudes, the weight matrix in q, q'-space is mostly diagonal. Especially without interaction, quantum entanglement between unlike states is rather implausible. But also along the diagonal, the weights are much more distributed for $U = 0$ simply because there is no interaction-driven state selection but only statistics of a Fermi gas. Since describing half-filling, for $U = 7$ eV the fluctuations in the 0,1 and 5,6 particle sectors are significantly suppressed. The truly relevant diagonal Fock states are easily selected [see Fig. 8(c)], using the notation

$$|q\rangle = |\uparrow_{z^2}\downarrow_{z^2}\uparrow_{x^2-y^2}\downarrow_{x^2-y^2}\uparrow_{\text{SD}}\downarrow_{\text{SD}}\rangle. \tag{5}$$

Not surprisingly, the largest weight stems from the $|111000\rangle$ and $|110100\rangle$ states in the three-particle sector, i.e., two electrons in Ni-d_{z^2} and one in Ni-$d_{x^2-y^2}$. Of course, doubly occupied (sub)states in Ni-$d_{x^2-y^2}$, though appreciated without interactions, are highly suppressed at large U. There are still four relevant diagonal states for $U = 7$ eV in the two- and four-particle sectors, respectively. The ones in the two-particle sector display Hund's first rule within Ni-e_g. The ones in the four-particle sector exhibit fully occupied Ni-d_{z^2} as well as singly occupied Ni-$d_{x^2-y^2}$ and SD but, importantly, without spin-alignment differentiation for the $|\phi_{qq'}|^2$ magnitude. In other words, without charge fluctuation in Ni-d_{z^2}, there is no exchange-favored discrimination of $\{\text{Ni-}d_{x^2-y^2}, \text{SD}\}$ spin states.

Finally, let us turn to the off-diagonal slave-boson weights, of which there are a few in the strongly interacting regime with sizable magnitude [cf. Figs. 8(b) and 8(c)] but still much smaller than the diagonal ones. There is a prominent $\phi_{qq'}$ in the two-particle sector, connecting the two Ni-e_g states $|100100\rangle$ and $|011000\rangle$, which clearly marks the relevant singlet $S = 0, S_z = 0$ and triplet $S = 1, S_z = 0$ entanglement in the e_g manifold. The respective twofold off-diagonal weights $\alpha^{(\prime)}$, $\beta^{(\prime)}$, and $\gamma^{(\prime)}$ in the three-particle sector are more complicated but most interesting. For clarity, let us enumerate them.

$\alpha^{(\prime)}$: scattering between doubly Ni-d_{z^2}, spin-up (down) Ni-$d_{x^2-y^2}$ and spin-up (down) Ni-d_{z^2}, spin-down (up) Ni-$d_{x^2-y^2}$, spin-down (up) SD.

$\beta^{(\prime)}$: scattering between singlet (triplet) Ni-d_{z^2}, Ni-$d_{x^2-y^2}$ and spin-up (down) SD.

$\gamma^{(\prime)}$: scattering between doubly Ni-d_{z^2}, spin-up (down) Ni-$d_{x^2-y^2}$ and spin-up (down) Ni-d_{z^2}, spin-up(down) Ni-$d_{x^2-y^2}$, spin-down (up) SD.

Thus, these weights provide the desired spin differentiation in the scattering processes between the three orbitals, relevant for paving the way toward establishing a proper Kondo(-lattice) picture. Accordingly, the weights scale as $\gamma^{(\prime)} > \alpha^{(\prime)} > \beta^{(\prime)}$, which, importantly, provides further quantitative evidence for a Hund-assisted Kondo scenario via Ni-d_{z^2}, leading to AFM exchange between localized Ni-$d_{x^2-y^2}$ and the SD band.

To conclude this discussion at stoichiometry, we comment on the role of the potential shift μ_{SD}, which has so far been set to $\mu_{\text{SD}} = U/2$. Figure 9 depicts the modifications in the electronic states by varying μ_{SD} to smaller and larger values. Generally, the effects from changing μ_{SD} by reasonable amounts are comparatively weak. The given potential shift defines the energy location of the SD band; thus, a smaller (larger) value shifts it upwards (downwards) with respect to $\mu_{\text{SD}} = U/2$ [see Fig. 9(a)]. Understandably, a larger μ_{SD} leads to a stronger filling of the SD band and to a decrease of correlation strength in Ni-$d_{x^2-y^2}$ [see Fig. 9(b)]. The growth of the $\{\text{Ni-}d_{z^2}, \text{Ni-}d_{x^2-y^2}\}$ spin-spin correlation with increasing μ_{SD} in Fig. 9(c) may be attributed to the less-filled Ni-d_{z^2} in this situation, strengthening the Ni-d_{z^2} moment. Furthermore, the μ_{SD} variation renders the coupling between itinerant and local degrees of freedom obvious. Figure 9(c) shows, for instance, the growth of an off-diagonal $|\phi_{qq'}|^2$ near the diagonal at the upper end of the four-particle sector. This growth amounts to the coupling of states $\{|011011\rangle, |100111\rangle\}$, describing scattering between singlet or triplet Ni-e_g and doubly occupied SD. Thus, the growth of SD occupation from a corresponding band that sinks below the Fermi level also leads to an increase of $\phi_{qq'}$ amplitudes associated with a completely filled SD state.

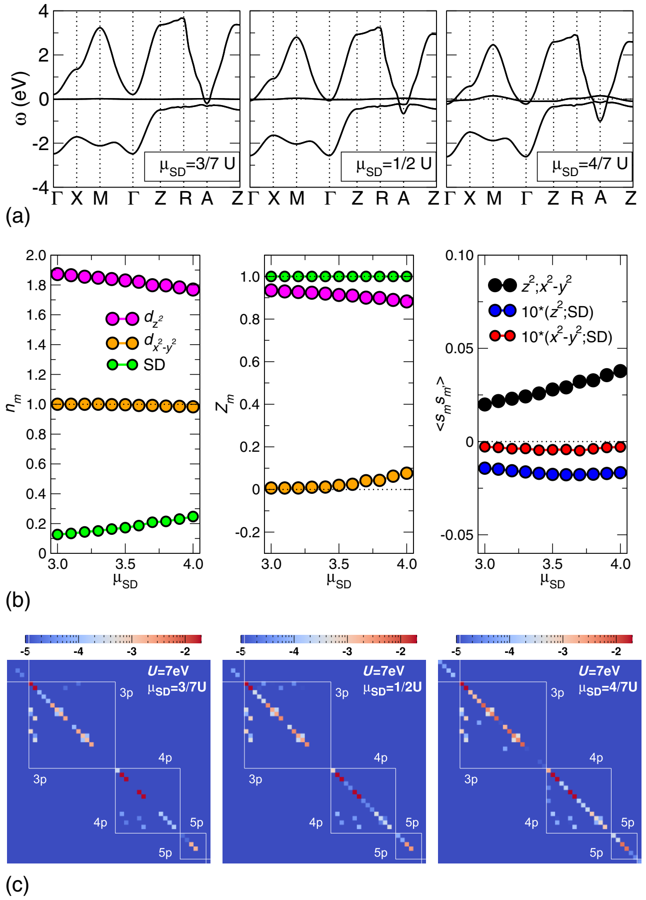

FIG. 9. Effect of μ_{SD} on the electronic states for $U = 7$ eV. (a) QP dispersion. (b) Orbital-resolved occupations, QP weights, and local spin-spin correlations. (c) Slave-boson weight matrix $|\phi_{qq'}|^2$ in higher particle sectors.

The observed μ_{SD} variations provide confidence that at stoichiometry, the setting $\mu_{\text{SD}} = U/2$ indeed proves reasonable. For instance, the existence of the Γ electron-pocket Fermi surface is a robust feature of the DFT + sicDMFT study (also reported from many other theoretical works).

2. Hole doping

The experimental doping with Sr, and, accordingly, the replacement of Nd^{3+} by Sr^{2+}, leads to the doping of holes into the nickelate compound. In Ref. [11], we studied this doping process by a DFT + sicDMFT treatment of realistic supercells for $Nd_{1-x}Sr_xNiO_2$ at $T = 193$ K. It was found that for $x = 0.125$, while both Ni-e_g orbitals gain holes (though Ni-d_{z^2} gains slightly more), the lowest-energy response comes mainly from Ni-$d_{x^2-y^2}$. However, for $x = 0.25$, the number of holes in Ni-d_{z^2} is quite large, and the lowest-energy response is twofold but dominated by Ni-d_{z^2}. This case is apparently not in line with the cupratelike, single-orbital, hole doping of Ni-$d_{x^2-y^2}$.

In the following, hole doping is investigated in more detail from the low-energy perspective within the minimal-Hamiltonian approach. It amounts to changing the total filling to $n = 3 - \delta$, with $\delta > 0$. This approach surely misses some effects of the realistic Nd substitution by Sr, but it should be geared to unveil the key qualitative features with doping. For instance, one (also electrostatic-supported) effect of true Sr doping is the shifting of the Γ electron pockets into the unoccupied region [11,20,21,27]. In the minimal-Hamiltonian scheme, part of the corresponding underlying mechanism surely goes into the value of μ_{SD}. Hence, we use the two values $\mu_{\mathrm{SD}} = 3/7U$ and $U/2$ for comparison and to correctly include that upward shifting qualitatively.

Figure 10 summarizes the key changes with hole doping from the minimal-Hamiltonian perspective for $U = 7$ eV. Notably, the differences between $\mu_{\mathrm{SD}} = 3/7U$ and $U/2$ are small and mostly quantitative. The first surprising (though already suggested by DFT + sicDMFT) observation is the very weak change of the Ni-$d_{x^2-y^2}$ orbital filling with increasing δ [cf. Fig 10(a)]. It remains very near half-filling up to the investigated limiting value $\delta = 0.4$. In fact, starting from stoichiometry, $n_{x^2-y^2}$ first decreases slightly until $\delta \sim 0.1$, and afterwards, it increases progressively toward half-filling. On the other hand, n_{z^2} decreases steadily with δ. The second surprise is the *increase* of the SD filling with hole doping. As one associates the electron pockets with SD, one naively expects a δ-induced depopulation of that orbital. However, one has to recall the important fact that the SD state hybridizes substantially with Ni-d_{z^2} over a large energy region (see bottom-right diagram of Fig. 6). With large U on Ni, the e_g electrons try hard to escape to the SD state if they cannot achieve complete localization. Hence, there is a correlation-induced change of the hybridization, apparently activated here for hole doping, such that the SD state increases its weight on the deep-lying Ni-d_{z^2}-dominated band and more electrons can benefit from the favorable SD-orbital location. This mechanism is proven by $Z_{z^2,\mathrm{SD}}$ being the only sizable off-diagonal QP weight, and its absolute value steadily increasing with δ [see bottom of Fig. 10(b)]. This off-diagonal Z monitors the outlined intersite hybridization modification between Ni-d_{z^2} and the SD state. Thus, the strong doping of Ni-d_{z^2} is triggered by the direct hole creation from δ, as well as by additional charge transfer to the SD state. This process is apparently energetically more favorable than putting more holes in Ni-$d_{x^2-y^2}$.

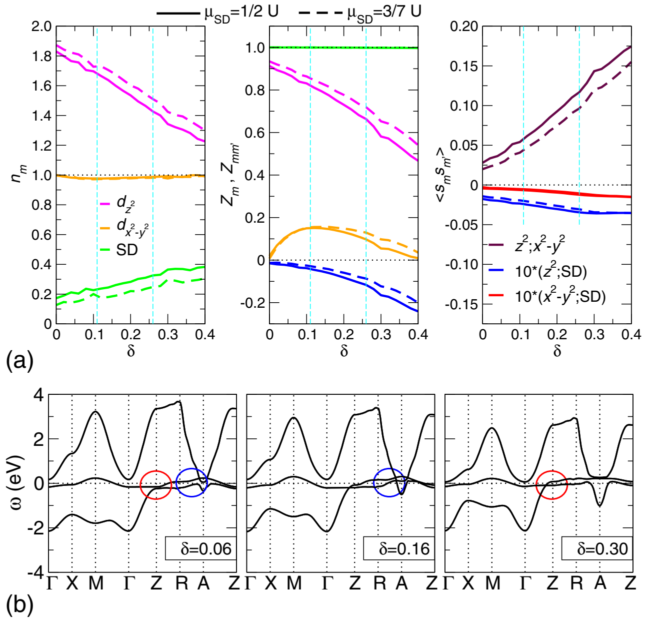

FIG. 10. Evolution of $NdNiO_2$ many-body electronic structure with hole doping δ, approached by the three-orbital Hamiltonian at $U = 7$ eV. (a) From left to right: Orbital-resolved occupations, QP weights, and local spin-spin correlations for $\mu_{\mathrm{SD}} = 3/7U$ (dashed lines) and $\mu_{\mathrm{SD}} = U/2$ (solid lines). Cyan dashed lines mark the occurrence of Fermi-surface reconstructions (see text). (b) QP dispersions at selected δ for $\mu_{\mathrm{SD}} = 3/7U$. Locations for the Fermi-surface reconstructions are highlighted by the blue ellipse (for those occurring at $\delta = 0.11$) and by the red ellipse (for those occurring at $\delta = 0.26$).

The diagonal QP weights Z_m behave as expected with δ, i.e., Z_{z^2} decreasing and $Z_{x^2-y^2}$ exhibiting a nonmonotonic behavior with a maximum around $\delta \sim 0.1$. Note again that the Ni-$d_{x^2-y^2}$ correlation strength at the large doping of $\delta \sim 0.4$ becomes comparable to the one at half-filling. Expectedly, the spin-spin correlation between the Ni-e_g orbitals increases with δ due to the enhancement of the Ni-d_{z^2} localization.

The described evolutions in fillings and many-body observables are accompanied by obvious changes of the interacting Fermi surface, shown in Fig. 10(b). For $\delta < 0.11$, the fermiology in the $k_z = 1/2$ plane is basically equivalent to the stoichiometric scenario, i.e., showing an electronlike pocket around Z [see right part of Fig. 7(c)]. Yet, for $\delta > 0.11$, there is a Lifshitz transition with an emerging second pocket around A. This pocket should not be confused with the original small SD-based electron pocket. The Lifshitz transition is realized by a doping- and correlation-induced shift of the rather flat Ni-d_{z^2}-dominant dispersion in the $k_z = 1/2$ plane onto the Fermi level. Note that already at stoichiometry, the enhanced proximity of the latter dispersion to ε_{F} compared to IL cuprates has been documented within LDA [11] and was also revealed within DFT + U [24].

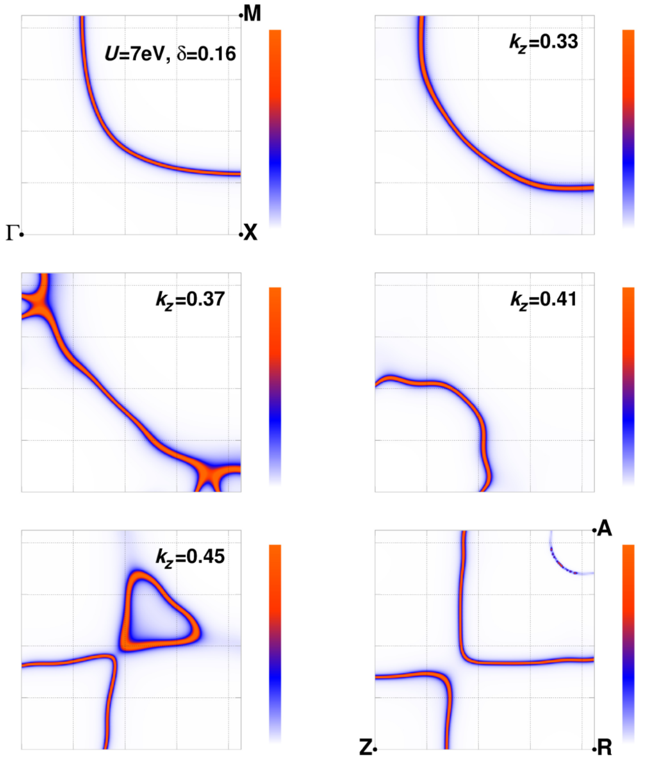

FIG. 11. Interacting Fermi surface along k_z at $\delta = 0.16$, for $U = 7$ eV and $\mu_{\mathrm{SD}} = 3/7U$.

Hence, the Fermi surface is reconstructed at $\delta \sim 0.11$, giving rise to the topology shown in Fig. 11 for $\delta = 0.16$. Moving along k_z, the original Ni-$d_{x^2-y^2}$ hole pocket bends over toward an electron pocket, shown for $k_z = 0.41$. At $k_z = 0.45$, a new heart-shaped hole pocket starts out along the nodal line. It opens up to a large hole sheet around A at $k_z = 1/2$. The nature of the novel larger pocket around A is of the mixed Ni-e_g kind. There is still another Lifshitz transition at larger δ. For $\delta < 0.26$, the van Hove singularity at Z lies below the Fermi level, and above for $\delta > 0.26$. Therefore, the $k_z = 1/2$ pocket around Z vanishes for hole doping beyond $\delta = 0.26$. It is surely tempting to relate these reconstructions with the experimental phase boundaries of superconductivity [2,4].

The **k**-integrated orbital-resolved QP spectral functions shown in Fig. 12 for selected dopings underline the scenario we just discussed: For $\delta = 0.06$, the Ni-d_{z^2} weight at the Fermi level is still small, whereas for $\delta = 0.16$, it is larger than Ni-$d_{x^2-y^2}$ and peaks at ϵ_{F}. The latter intermediate region therefore displays the strongest susceptibility for Ni-d_{z^2}-driven instabilities in a highly localized Ni-$d_{x^2-y^2}$ background. For $\delta = 0.30$, the Ni-d_{z^2} weight close to ϵ_{F} is again smaller, since the Fermi level is located in a "pseudogap" of Ni-d_{z^2} weight. This structure is well understood from Ni-d_{z^2} occupation of states with small k_z and unoccupied states with k_z closer to $1/2$, due to the doping-dependent QP band shifts.

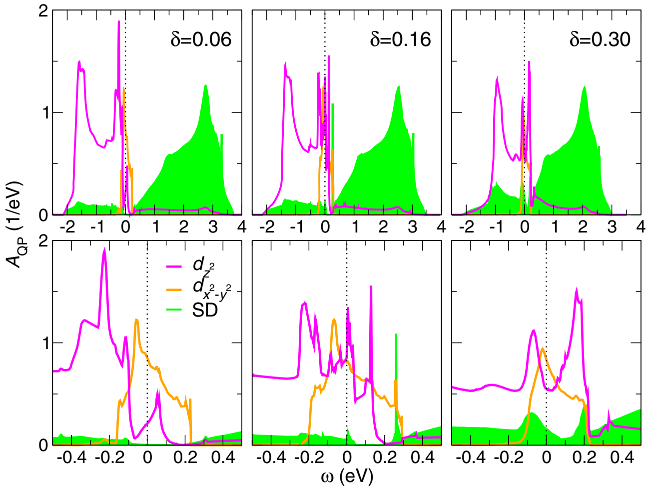

FIG. 12. Orbital-resolved **k**-integrated QP dispersion for selected hole dopings δ based on the minimal-Hamiltonian approach. Top (bottom): Wide (narrow) energy window. Since there are no Hubbard bands in mean-field RISB, note that each orbital spectrum is multiplied by the respective Z_m to account for the proper relative QP weight.

A further complexity issue has to be discussed. Upon increasing δ and running through the described Fermi surface reconstructions, the character partition between Ni-d_{z^2} and Ni-$d_{x^2-y^2}$ on the (near-)$k_z = 1/2$ Fermi sheets also varies because the original bands of both orbital characters sweep through each other in that region of the Brillouin zone with doping [see Fig. 7(b)]. Hence, a nontrivial mixing of characters due to correlation-modified hybridizations takes place. Table II summarizes the basic information in simple terms for selected dopings in the three distinct regions. We see that the intermediate doping region $0.11 < \delta < 0.26$ displays the most intriguing case with the strongest multiorbital character of the Fermi surface. Note that the issue of mixed Fermi-surface character does not arise in the $k_z = 0$ plane: The $\Gamma - \mathrm{M}$ pocket is of a perfect Ni-$d_{x^2-y^2}$ kind throughout the studied hole-doping region.

In fact, recent experimental Hall data in the normal state are interpreted as going from an electronlike to a holelike transport scenario with doping [2,4]. This interpretation is in line with our findings since, for small δ, transport should

TABLE II. Qualitative orbital-character strength on the interacting Fermi-surface sheets in the $k_z = 1/2$ plane for selected hole dopings. See bottom right of Fig. 11 for a visualization of both Fermi sheets.

Orbital	Fermi sheets	$\delta = 0.06$	$\delta = 0.16$	$\delta = 0.30$
Ni-d_{z^2}	Around Z	Moderate	Strong	$\cdots$
	Around A	$\cdots$	Moderate	Weak
Ni-$d_{x^2-y^2}$	Around Z	Strong	Moderate	$\cdots$
	Around A	$\cdots$	Moderate	Strong

mainly arise from the vanishing SD electron pockets and the electronlike bent region around Z, which has mixed Ni-e_g character (cf. Table II). But for $\delta > 0.11$, the hole pocket around A appears, showing sizable Ni-d_{z^2} weight for intermediate doping.

Last but not least, the present results allow us to also provide an explanation for the puzzling, weakly insulating behavior for $x > 0.25$ in experiment [2,4]. First, the SD electron pockets are above the Fermi level at larger hole doping. Second, Ni-$d_{x^2-y^2}$ remains essentially half-filled and localized for large δ; the $k_z = 0$ Fermi sheet is Ni-$d_{x^2-y^2}$ dominated and thus is the only one remaining in the $k_z = 1/2$ plane (see Table II for $\delta = 0.30$). Thus, transport from that orbital sector is, by any means, very weak at larger δ. Third, the only remaining Fermi sheet with strong Ni-d_{z^2} character for large δ lies *along* k_z, i.e., between $\Gamma - Z$ [see Fig. 10(c) for $\delta = 0.30$]. But that sheet will mainly account for transport in the c-axis direction of a $Nd_{1-x}Sr_xNiO_2$ crystal. Yet transport measurements have so far been performed on thin films. In summary, in-plane conductivity at hole dopings beyond the upper superconducting phase boundary is indeed expected to be very weak from our theoretical study.

The δ variation of the Ni-e_g multiorbital character is schematically sketched in Fig. 13, where the doping-dependent Fermi-surface sheets are counted with respect to their participation of either of the Ni-e_g flavors. It is seen that the intermediate region of hole doping, which interestingly agrees rather well with the experimental region for superconductivity, is designated with the most pronounced multiorbital character.

3. Comparison between electron and hole doping

The dichotomy between electron and hole doping is an essential part of the high-T_c cuprates physics [58]. Therefore, in the final section, we compare, in basic terms, the electron-doped region within the minimal-Hamiltonian approach with the hole-doped one. Experimentally, electron doping of $NdNiO_2$ has not been achieved yet. In analogy to cuprates, it could formally be realized by, e.g., replacing Nd^{3+} with Ce^{4+}. The theoretical calculations are straightforwardly extended to electron doping by fixing the total particle number at $n = 3 - \delta$ with $\delta < 0$.

Figure 14 displays the comparison of both doping regimes. We lower the Hubbard interaction to $U = 6$ eV since the RISB numerics of the electron-doped region turns out to be more challenging. Nonetheless, the hole-doped side behaves qualitatively identical to $U = 7$ eV.

Let us thus focus on the electron doping, which shows singular differences from hole doping. Starting with the QP weights, it is seen that for small δ, the correlation strength in Ni-$d_{x^2-y^2}$ apparently *increases* compared to half-filling. After a minimum at $\delta \sim -0.1$, the QP weight $Z_{x^2-y^2}$ then strongly recovers and increases to the limiting value $\delta = -0.4$. The doping $\delta = -0.1$ apparently marks the true orbital-selective Mott-transition point in the IL nickelate. The Ni-$d_{x^2-y^2}$ filling remains fixed at half-filling for small δ, but then it grows beyond the latter transition point. Expectedly, the Ni-d_{z^2} orbital has to accommodate even more electrons with electron doping. Yet, because of the large associated Coulomb-repulsion cost, it succeeds in not becoming completely filled but can delegate some charge to the remaining orbitals. It is also not surprising that the SD orbital becomes further filled, too. With electron doping, no sophisticated correlation-induced change of hybridization has to be invoked in order to place additional electrons in the SD state. Correspondingly, the off-diagonal QP weight $Z_{z^2,\mathrm{SD}}$ is small for electron doping. Thus, albeit original electron pockets of the SD band shift deeper into the occupied region, the coupling, at least to Ni-d_{z^2}, appears weaker. The Ni-e_g spin-spin correlations are much smaller for electron doping because of the even stronger Ni-d_{z^2} filling. Interestingly, when adding electrons, the spin-spin correlations between Ni-$d_{x^2-y^2}$ and SD change sign from negative to positive at the critical point $\delta = -0.1$.

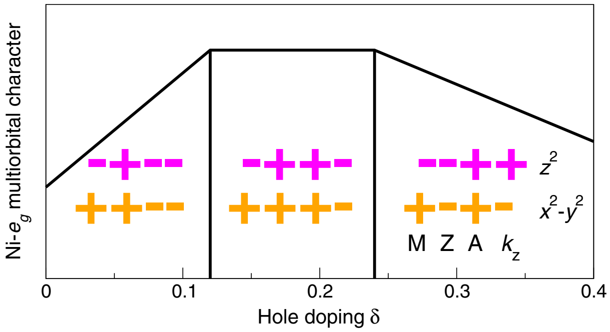

FIG. 13. Schematic sketch of the Ni-e_g multiorbital character with δ. The "+" symbols denote a Fermi-sheet participation of $x^2 - y^2$ or z^2, respectively, around M, Z, A or along k_z in the Brillouin zone.

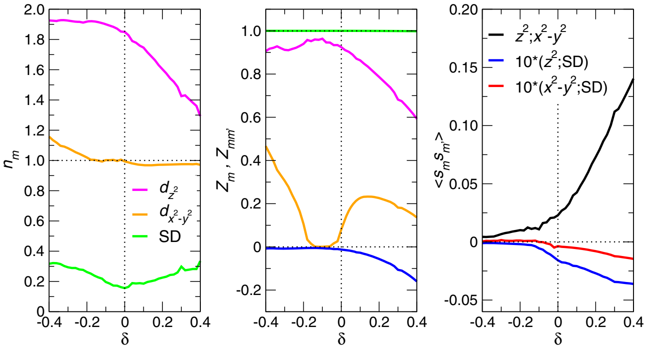

FIG. 14. Comparison of electron ($\delta < 0$) vs hole ($\delta > 0$) doping within the minimal-Hamiltonian picture for $U = 6$ eV. From left to right: Orbital-resolved occupations, QP weights, and local spin-spin correlations. The SD potential shift is set to $\mu_{\mathrm{SD}} = U/2$.

The electron-doped region might be interesting because of obviously stronger Ni-$d_{x^2-y^2}$ correlation at low doping and possibly intriguing competition between Kondo correlations and magnetic order. Superconducting tendencies like those on the hole-doped side are not expected since electron doping should not lead to comparable intricate Fermi-surface reconstructions as Ni-d_{z^2} becomes too strongly filled. However, apparently, the electron-doped side supports a stronger Ni single-orbital picture of the Ni-$d_{x^2-y^2}$ kind. Thus, despite the coexistence with the remaining SD band, similarities to cuprates might be more pronounced with electron doping.

V. SUMMARY AND DISCUSSION

Using comprehensive DFT + sicDMFT, as well as an aligned minimal-Hamiltonian representation solved within RISB, we were able obtain important insight into the very rich physics of $\mathrm{NdNiO_2}$ in pristine conditions and with finite doping.

Relevant features of a stoichiometric Kondo(-lattice) scenario at lower temperature are revealed, showing that a calculated, sizable, AFM Kondo coupling $J_{\mathrm{K}} \sim 120$ meV builds onto the cooperation of Ni-$d_{x^2-y^2}$, Ni-d_{z^2}, and the self-doping band. The Ni-d_{z^2} and the SD band both take part in the screening of the Ni-$d_{x^2-y^2}$ spin, whereby the former orbital has a mediating role through a Hund-assisting mechanism. The onset of significant Kondo correlations around $T \sim 60$ K matches well with the experimental $T = 70$ K for the beginning resistivity upturn [1]. An interesting $\mathbf{k}$-selective Ni-e_g hybridization via oxygen around Γ deserves further investigation.

A realistic minimal three-orbital Hamiltonian is advocated, which describes the low-energy competition of both Ni-e_g orbitals linked to a SD state that carries the effect of the remaining Nd($5d$), O($2p$), Ni-t_{2g}, and Ni($4s$). This Hamiltonian serves the goal of providing a faithful representation of the key degrees of freedom of IL nickelate. Its canonical structure, i.e., two strongly interacting orbitals coupled to a stand-alone bath state, may prove useful for other nickelates or related problems.

The system with hole doping δ is remarkably different from hole-doped cuprates. The Ni-$d_{x^2-y^2}$ occupation only very weakly departs from half-filling, and the orbital even regains correlation strength at larger δ. On the other hand, the Ni-d_{z^2} orbital eagerly collects holes—also at the expense of the SD orbital, which counterintuitively gains electrons by a correlation-induced change of hybridization to Ni-d_{z^2}. While the QP weight for the latter orbital decreases with δ, it remains in a weak-to-moderate correlation regime of $Z_{z^2} \sim 0.7$ at intermediate doping. Further key aspects at hole doping are two apparent Fermi-surface constructions that designate $0.11 < \delta < 0.26$ as the region with the strongest multiorbital nature and entanglement. It is an orbital-selective(-kind) situation with highly correlated, hardly doped Ni-$d_{x^2-y^2}$ and still substantially filled Ni-d_{z^2} sharing two Fermi sheets in the $k_z = 1/2$ plane of the Brillouin zone. This specific doping region agrees well with the two experimentally determined ranges, i.e., $0.125 < x < 0.25$ by Li *et al.* [2] and $0.12 < x < 0.235$ by Zeng *et al.* [4], for the appearance of superconductivity in $\mathrm{Nd_{1-x}Sr_xNiO_2}$.

Moreover, our realistic description may not only explain the experimentally observed change from electronlike to holelike transport in Hall measurements, but it may also provide a reason for the weakly insulating behavior found on *both* sides of the superconducting region. In essence, Ni-$d_{x^2-y^2}$ remains nearly localized for any reasonable hole doping, and the itinerant contribution of Ni-d_{z^2} remains generally small for $\delta < 0.11$ while contributing mostly to c-axis transport for $\delta > 0.26$. The latter should be masked in the available thin-film studies of $\mathrm{Nd_{1-x}Sr_xNiO_2}$.

Finally, theoretical electron doping leads to quite different characteristics than hole doping. Most notably, even further correlation-strength enhancement within Ni-$d_{x^2-y^2}$ is found for small negative δ, and the spin exchange between the latter and the SD orbital switches to ferrolike behavior. The predominant Ni-$d_{x^2-y^2}$ characteristics on the electron-doped side deserve further experimental investigation.

The present theoretical results raise several further questions. For instance, one wonders about the role of Ni-t_{2g} states with hole doping since those are also located close to the Fermi level. However, from our defect-supercell DFT + sicDMFT study [11], which included all Ni($3d$) on equal footing, they become only weakly doped, and their contribution to relevant low-energy physics appears minor up to $x \sim 0.25$. An intuitive reason for this case may be given by the fact that, already at the LDA level, Ni-e_g more strongly disperses than Ni-t_{2g}. At strong coupling, with Ni-$d_{x^2-y^2}$ becoming half-filled, the only appreciable itinerant Ni($3d$) degree of freedom to balance the electronic energy cost is thus provided by Ni-d_{z^2}. Second, if the IL nickelate superconductivity is based on multiorbital Ni-e_g processes and not on the singular cuprate mechanism, the question arises as to why stable pairing is not much more common in nickel-based transition-metal oxides. Yet, one has to be aware that the orbital-selective(-like) scenario allied with intriguing fermiology in the intermediate doping region is quite specific; to our knowledge, it has not yet been reported for other nickelates, which brings us to the most pressing question concerning the pairing mechanism that emerges from the present normal-state scenario. A straightforward, simple answer is not available because of the complex entanglement between localized and itinerant multiorbital degrees of freedom. From the renormalized-band perspective, a nesting mechanism involving the flattened, larger, hole-pocket sheets around A might be conceivable. From a more localized perspective, recent suggestions based on Ni-e_g couplings have been put forward [9,10]. However, those interesting proposals miss the details of the intricate low-energy dispersions that evidently mark the intermediate doping region.

Beyond speculations, as the main conclusion, the superconductivity in thin films of $\mathrm{Nd}_{1-x}\mathrm{Sr}_x\mathrm{NiO}_2$ is most definitely not of the single-orbital cuprate kind. This conclusion can be appreciated as the opening of a new fascinating chapter on the research of superconducting correlated materials.

ACKNOWLEDGMENTS

The author thanks K. Held, H. Y. Hwang, A. I. Lichtenstein, L. de' Medici, A. J. Millis, and P. Werner for helpful discussions. Financial support from the German Science Foundation (DFG) via Project No. LE-2446/4-1 is gratefully acknowledged. This work benefited from discussions held at the Aspen Center for Physics, which is supported by National Science Foundation Grant No. PHY-1607611. Computations were performed at the University of Hamburg and the JUWELS Cluster of the Jülich Supercomputing Centre (JSC) under Project No. hhh08.

[1] D. Li, K. Lee, B. Y. Wang, M. Osada, S. Crossley, H. R. Lee, Y. Cui, Y. Hikita, and H. Hwang, *Superconductivity in an Infinite-Layer Nickelate*, Nature (London) **572**, 624 (2019).

[2] D. Li, B. Y. Wang, K. Lee, S. P. Harvey, M. Osada, B. H. Goodge, L. F. Kourkoutis, and H. Y. Hwang, *Superconducting Dome in* $\mathrm{Nd}_{1-x}\mathrm{Sr}_x\mathrm{NiO}_2$ *Infinite Layer Films*, Phys. Rev. Lett. **125**, 027001 (2020).

[3] K. Lee, B. H. Goodge, D. Li, M. Osada, B. Y. Wang, Y. Cui, L. F. Kourkoutis, and H. Y. Hwang, *Aspects of the Synthesis of Thin Film Superconducting Infinite-Layer Nickelates*, APL Mater. **8**, 041107 (2020).

[4] S. Zeng, C. S. Tang, X. Yin, C. Li, Z. Huang, J. Hu, W. Liu, G. J. Omar, H. Jani, Z. S. Lim, K. Han, D. Wan, P. Yang, A. T. S. Wee, and A. Ariando, *Phase Diagram and Superconducting Dome of Infinite-Layer* $\mathrm{Nd}_{1-x}\mathrm{Sr}_x\mathrm{NiO}_2$ *Thin Films*, arXiv:2004.11281.

[5] Y. Gu, S. Zhu, X. Wang, J. Hu, and H. Chen, *Hybridization and Correlation Effects in the Electronic Structure of Infinite-Layer Nickelates*, Commun. Phys. **3**, 84 (2020).

[6] M. Hepting *et al.*, *Electronic Structure of the Parent Compound of Superconducting Infinite-Layer Nickelates*, Nat. Mater. **19**, 381 (2020).

[7] L.-H. Hu and C. Wu, *Two-Band Model for Magnetism and Superconductivity in Nickelates*, Phys. Rev. Research **1**, 032046 (2019).

[8] H. Zhang, L. Jin, S. Wang, B. Xi, X. Shi, F. Ye, and J.-W. Mei, *Effective Hamiltonian for Nickelate Oxides* $\mathrm{Nd}_{1-x}\mathrm{Sr}_x\mathrm{NiO}_2$, Phys. Rev. Research **2**, 013214 (2020).

[9] Y.-H. Zhang and A. Vishwanath, *Type II* $t-J$ *Model in Superconducting Nickelate* $\mathrm{Nd}_{1-x}\mathrm{Sr}_x\mathrm{NiO}_2$, Phys. Rev. Research **2**, 023112 (2020).

[10] P. Werner and S. Hoshino, *Nickelate Superconductors—Multiorbital Nature and Spin Freezing*, Phys. Rev. B **101**, 041104(R) (2020).

[11] F. Lechermann, *Late Transition Metal Oxides with Infinite-Layer Structure: Nickelates versus Cuprates*, Phys. Rev. B **101**, 081110(R) (2020).

[12] T. Zhou, Y. Gao, and Z. D. Wang, *Spin Excitations in Nickelate Superconductors*, Sci. China Phys. Mech. Astron. **63**, 287412 (2020).

[13] J. Hirsch and F. Marsiglio, *Hole Superconductivity in Infinite-Layer Nickelates*, Physica C **566**, 1353534 (2019).

[14] Z. Liu, Z. Ren, W. Zhu, Z. F. Wang, and J. Yang, *Electronic and Magnetic Structure of Infinite-Layer* NdNiO_2*: Trace of Antiferromagnetic Metal*, npj Quantum Mater. **5**, 31 (2020).

[15] M. Jiang, M. Berciu, and G. A. Sawatzky, *Doped Holes in* NdNiO_2 *and High-*T_c *Cuprates Show Little Similarity*, Phys. Rev. Lett. **124**, 207004 (2020).

[16] P. Jiang, L. Si, Z. Liao, and Z. Zhong, *Electronic Structure of Rare-Earth Infinite-Layer* $R\mathrm{NiO}_2(R = \mathrm{La}, \mathrm{Nd})$, Phys. Rev. B **100**, 201106(R) (2019).

[17] S. Ryee, H. Yoon, T. J. Kim, M. Y. Jeong, and M. J. Han, *Induced Magnetic Two-Dimensionality by Hole Doping in Superconducting* $\mathrm{Nd}_{1-x}\mathrm{Sr}_x\mathrm{NiO}_2$, Phys. Rev. B **101**, 064513 (2020).

[18] X. Wu, D. D. Sante, T. Schwemmer, W. Hanke, H. Y. Hwang, S. Raghu, and R. Thomale, *Robust* $d_{x^2-y^2}$*-Wave Superconductivity of Infinite-Layer Nickelates*, Phys. Rev. B **101**, 060504(R) (2020).

[19] Y. Nomura, M. Hirayama, T. Tadano, Y. Yoshimoto, K. Nakamura, and R. Arita, *Formation of 2D Single-Component Correlated Electron System and Band Engineering in the Nickelate Superconductor* NdNiO_2, Phys. Rev. B **100**, 205138 (2019).

[20] A. S. Botana and M. R. Norman, *Similarities and Differences between* LaNiO_2 *and* CaCuO_2 *and Implications for Superconductivity*, Phys. Rev. X **10**, 011024 (2020).

[21] G.-M. Zhang, Y.-F. Yang, and F.-C. Zhang, *Self-Doped Mott Insulator for Parent Compounds of Nickelate Superconductors*, Phys. Rev. B **101**, 020501(R) (2020).

[22] L. Si, W. Xiao, J. Kaufmann, J. M. Tomczak, Y. Lu, Z. Zhong, and K. Held, *Topotactic Hydrogen in Nickelate Superconductors and Akin Infinite-Layer Oxides* $AB\mathrm{O}_2$, Phys. Rev. Lett. **124**, 166402 (2020).

[23] M. Kitatani, L. Si, O. Janson, R. Arita, Z. Zhong, and K. Held, *Nickelate Superconductors—A Renaissance of the One-Band Hubbard Model*, arXiv:2002.12230.

[24] M.-Y. Choi, K.-W. Lee, and W. E. Pickett, *Role of* $4f$ *States in Infinite-Layer* NdNiO_2, Phys. Rev. B **101**, 020503(R) (2020).

[25] J. Karp, A. S. Botana, M. R. Norman, H. Park, M. Zingl, and A. Millis, *Many-Body Electronic Structure of* NdNiO_2 *and* CaCuO_2, Phys. Rev. X **10**, 021061 (2020).

[26] V. Olevano, F. Bernardini, X. Blase, and A. Cano, *Ab Initio Many-Body GW Correlations in the Electronic Structure of* LaNiO_2, Phys. Rev. B **101**, 161102(R) (2020).

[27] I. Leonov, S. L. Skornyakov, and S. Y. Savrasov, *Lifshitz Transition and Frustration of Magnetic Moments in Infinite-Layer* NdNiO_2 *upon Hole-Doping*, Phys. Rev. B **101**, 241108(R) (2020).

[28] E. Been, W.-S. Lee, H. Y. Hwang, Y. Cui, J. Zaanen, T. Devereaux, B. Moritz, and C. Jia, *Theory of Rare-Earth Infinite Layer Nickelates*, arXiv:2002.12300.

[29] E. M. Nica, J. Krishna, R. Yu, Q. Si, A. S. Botana, and O. Erten, *Theoretical Investigation of Superconductivity in Trilayer Square-Planar Nickelates*, Phys. Rev. B **102**, 020504(R) (2020).

[30] V. I. Anisimov, D. Bukhvalov, and T. M. Rice, *Electronic Structure of Possible Nickelate Analogs to the Cuprates*, Phys. Rev. B **59**, 7901 (1999).

[31] K.-W. Lee and W. E. Pickett, *Infinite-Layer* $\mathrm{LaNiO_2}$*:* Ni^{1+} *Is Not* Cu^{2+}, Phys. Rev. B **70**, 165109 (2004).

[32] J. Chaloupka and G. Khaliullin, *Orbital Order and Possible Superconductivity in* $\mathrm{LaNiO_3/LaMO_3}$ *Superlattices*, Phys. Rev. Lett. **100**, 016404 (2008).

[33] P. Hansmann, X. Yang, A. Toschi, G. Khaliullin, O. K. Andersen, and K. Held, *Turning a Nickelate Fermi Surface into a Cupratelike One through Heterostructuring*, Phys. Rev. Lett. **103**, 016401 (2009).

[34] D. Grieger, C. Piefke, O. E. Peil, and F. Lechermann, *Approaching Finite-Temperature Phase Diagrams of Strongly Correlated Materials: A Case Study for* $\mathrm{V_2O_3}$, Phys. Rev. B **86**, 155121 (2012).

[35] F. Lechermann, W. Körner, D. F. Urban, and C. Elsässer, *Interplay of Charge-Transfer and Mott-Hubbard Physics Approached by an Efficient Combination of Self-Interaction Correction and Dynamical Mean-Field Theory*, Phys. Rev. B **100**, 115125 (2019).

[36] W. Körner and C. Elsässer, *First-Principles Density Functional Study of Dopant Elements at Grain Boundaries in ZnO*, Phys. Rev. B **81**, 085324 (2010).

[37] C. Elsässer, N. Takeuchi, K. M. Ho, C. T. Chan, P. Braun, and M. Fähnle, *Relativistic Effects on Ground State Properties of 4D and 5D Transition Metals*, J. Phys. Condens. Matter **2**, 4371 (1990).

[38] F. Lechermann, F. Welsch, C. Elsässer, C. Ederer, M. Fähnle, J. M. Sanchez, and B. Meyer, *Density-Functional Study of* $\mathrm{Fe_3Al}$*: LSDA versus GGA*, Phys. Rev. B **65**, 132104 (2002).

[39] B. Meyer, C. Elsässer, F. Lechermann, and M. Fähnle, *FORTRAN 90 Program for Mixed-Basis-Pseudopotential Calculations for Crystals*, Max-Planck-Institut für Metallforschung, Stuttgart (1998).

[40] A. Fujimori and F. Minami, *Valence-Band Photoemission and Optical Absorption in Nickel Compounds*, Phys. Rev. B **30**, 957 (1984).

[41] J. van Elp, H. Eskes, P. Kuiper, and G. A. Sawatzky, *Electronic Structure of Li-Doped NiO*, Phys. Rev. B **45**, 1612 (1992).

[42] M. Taguchi, M. Matsunami, Y. Ishida, R. Eguchi, A. Chainani, Y. Takata, M. Yabashi, K. Tamasaku, Y. Nishino, T. Ishikawa, Y. Senba, H. Ohashi, and S. Shin, *Revisiting the Valence-Band and Core-Level Photoemission Spectra of NiO*, Phys. Rev. Lett. **100**, 206401 (2008).

[43] P. Werner, A. Comanac, L. de' Medici, M. Troyer, and A. J. Millis, *Continuous-Time Solver for Quantum Impurity Models*, Phys. Rev. Lett. **97**, 076405 (2006).

[44] O. Parcollet, M. Ferrero, T. Ayral, H. Hafermann, I. Krivenko, L. Messio, and P. Seth, *TRIQS: A Toolbox for Research on Interacting Quantum Systems*, Comput. Phys. Commun. **196**, 398 (2015).

[45] P. Seth, I. Krivenko, M. Ferrero, and O. Parcollet, *TRIQS/CTHYB: A Continuous-Time Quantum Monte Carlo Hybridisation Expansion Solver for Quantum Impurity Problems*, Comput. Phys. Commun. **200**, 274 (2016).

[46] B. Amadon, F. Lechermann, A. Georges, F. Jollet, T. O. Wehling, and A. I. Lichtenstein, *Plane-Wave Based Electronic Structure Calculations for Correlated Materials Using Dynamical Mean-Field Theory and Projected Local Orbitals*, Phys. Rev. B **77**, 205112 (2008).

[47] V. I. Anisimov, I. V. Solovyev, M. A. Korotin, and M. T. Czyżyk, and G. A. Sawatzky, *Density-Functional Theory and NiO Photoemission Spectra*, Phys. Rev. B **48**, 16929 (1993).

[48] N. Marzari and D. Vanderbilt, *Maximally Localized Generalized Wannier Functions for Composite Energy Bands*, Phys. Rev. B **56**, 12847 (1997).

[49] I. Souza, N. Marzari, and D. Vanderbilt, *Maximally Localized Wannier Functions for Entangled Energy Bands*, Phys. Rev. B **65**, 035109 (2001).

[50] T. Li, P. Wölfle, and P. J. Hirschfeld, *Spin-Rotation-Invariant Slave-Boson Approach to the Hubbard Model*, Phys. Rev. B **40**, 6817 (1989).

[51] F. Lechermann, A. Georges, G. Kotliar, and O. Parcollet, *Rotationally Invariant Slave-Boson Formalism and Momentum Dependence of the Quasiparticle Weight*, Phys. Rev. B **76**, 155102 (2007).

[52] A. Isidori and M. Capone, *Rotationally Invariant Slave Bosons for Strongly Correlated Superconductors*, Phys. Rev. B **80**, 115120 (2009).

[53] N. Lanatà, Y. Yao, X. Deng, V. Dobrosaljević, and G. Kotliar, *Slave Boson Theory of Orbital Differentiation with Crystal Field Effects: Application to* $\mathrm{UO_2}$, Phys. Rev. Lett. **118**, 126401 (2017).

[54] C. Piefke and F. Lechermann, *Rigorous Symmetry Adaptation of Multiorbital Rotationally Invariant Slave-Boson Theory with Application to Hund's Rules Physics*, Phys. Rev. B **97**, 125154 (2018).

[55] J. I. Facio, J. Mravlje, L. Pourovskii, P. S. Cornaglia, and V. Vildosola, *Spin-Orbit and Anisotropic Strain Effects on the Electronic Correlations in* $\mathrm{Sr_2RuO_4}$, Phys. Rev. B **98**, 085121 (2018).

[56] Y.-F. Yang, Z. Fisk, H. O. Lee, J. D. Thompson, and D. Pines, *Scaling the Kondo Lattice*, Nature (London) **454**, 611 (2008).

[57] S. Schuwalow, C. Piefke, and F. Lechermann, *Impact of the Dzyaloshinskii-Moriya Interaction in Strongly Correlated Itinerant Systems*, Phys. Rev. B **85**, 205132 (2012).

[58] N. P. Armitage, P. Fournier, and R. L. Greene, *Progress and Perspectives on Electron-Doped Cuprates*, Rev. Mod. Phys. **82**, 2421 (2010).